**Tectonic controls on Ni and Cu contents of primary mantle-derived magmas for the formation of magmatic sulfide deposits**

Zhuosen Yao[a,b,d], Kezhang Qin[a,b,c*], James E. Mungall[d]

[a] Key Laboratory of Mineral Resources, Institute of Geology and Geophysics, Chinese Academy of Sciences, Beijing, 100029, China

[b] University of Chinese Academy of Sciences, Beijing 100049, China

[c] CAS Center for Excellence in Tibetan Plateau Earth Science, Beijing 100101, China

[d] Department of Earth Sciences, Carleton University, 1125 Colonel By Drive, Ottawa, ON K1S 5B6, Canada

* Corresponding author. E-mail address: kzq@mail.iggcas.ac.cn

# Supplementary Information

## 1. Various modeling approaches

As the existing experiments are far from sufficient to meet the needs of understanding the origin of primary magma and the associated partial melting process of mantle, many melting parameterizations (e.g., McKenzie and Bickle 1988; Langmuir et al. 1992; Kinzler and Grove 1992; Herzberg and O'Hara 2002; Katz et al. 2003; Till et al. 2012; Kimura and Kawabata 2014; Mungall and Brenan 2014) and/or thermodynamic models (e.g., Ghiorso 1994; Ghiorso and Sack 1995; Ghiorso et al. 2002; Connolly 2005; Holland and Powell 2011; Ueki and Iwamori 2013; Jennings and Holland 2015) have been presented.

Mostly, the melting parameterizations use empirical formulations of temperature, pressure, melt fraction and composition based on the existing experiments to model the partial melting of mantle peridotite (McKenzie and Bickle 1988; Langmuir et al. 1992; Kinzler and Grove 1992; Katz et al. 2003; Till et al. 2012; Mungall and Brenan 2014). As a result, the validity of these parameterizations strongly depends on the selection and update of the experimental database (Till et al. 2012; Grove et al. 2013). However, the thermodynamic constraints on such parameterizations should be important and even indispensable, because the experimental data for peridotite melting may show a large scatter (Katz et al. 2003). An alternative parameterized approach adopts the numerical mass balance calculations of incompatible trace elements between a source peridotite and the generated melt, e.g., the HAMMS1 (Kimura and Kawabata 2014) and ABS (Kimura et al. 2009, 2010); whereas, it requires pre-existing knowledge of the primary basalt compositions, so it is not a fully independent parameterization.

In contrast, several thermodynamic models were built up based on the minimization of free energy of melt-present system, e.g., MELTS, pMELTS, Perplex and THERMOCALC (Ghiorso et al. 2002; Connolly 2005; Holland and Powell 2011; Ueki and Iwamori 2013; Jennings and Holland 2015), using various energy minimization algorithms, thermodynamic configurations

and parameters. Among them, the pMELTS, as an important part of the alphaMELTS family, has been widely used to model the P-T conditions, melt compositions, phase relations of the partial melting of peridotite mantle at the pressure not greater than 4 GPa, via the fractional, continuous or equilibrium melting mechanisms, following isobaric, polybaric or dynamic P-T paths (Ghiorso 1994; Ghiorso and Sack 1995; Ghiorso et al. 2002; Asimow et al. 2004; Smith and Asimow 2005). However, due to the over-stabilization of clinopyroxene in pMELTS, the predicted temperature required to achieve a given melt fraction is ~50-60°C higher than experimental results (Ghiorso et al. 2002). At high pressure (3-7GPa), the pMELTS modeling further shows the over-stability of garnet and under-stability of olivine (Ghiorso et al. 2002). Recently, a new thermodynamic model with THERMOCALC (Powell et al. 1998) performs better in predicting mantle melts and phase relations, from 0.1 MPa to 6 GPa (Jennings and Holland 2015); however, the validity of this model is restricted to a narrow range of melt composition, and it can do nothing for the polybaric fractional melting. Therefore, we adopt the latest version of alphaMELTS with the updated models for garnet and spinel phases to track the dynamic partial melting of mantle at various tectonic settings; meanwhile caution is warranted in using the predicted results.

Here, we selected two anhydrous bulk compositions, ranging from relatively depleted MORB mantle (DMM1, Wasylenki et al. 2003) to fertile peridotite (MM-3, Baker and Stolper 1994; Baker et al. 1995; Falloon et al. 1999, 2001, 2008) to test the validity of the alphaMELTS model (Fig. S1). The calculated residual phase modes at different melting degrees closely match the experimental results for isobaric melting of fertile MM-3 and ultradepleted DMM1 at 1 GPa, especially the exhaustion of clinopyroxene (Figs. S1a and S1e). When pressure increases to 1.5 GPa, the reproducibility of the phase proportions of restite in alphaMELTS modeling for MM-3 is relatively poor in olivine and orthopyroxene (Fig. S1c). For the fertile MM-3, the temperature calculated using alphaMELTS is overestimated at the same melt fraction, whereas this discrepancy is strongly reduced when the melt fraction exceeds 20 wt.% (Figs. S1b and S1d). The reproducibility of alphaMELTS model is relatively poor for DMM1 at 1 GPa, showing that the predicted T vs. melt fraction trend plots above, but parallels to the experimental data (Fig. S1f). However, the discrepancy of temperature (~50°C) at the given melt fraction (Fig. S1f) is much smaller than the deviation calculated by the earlier version of pMELTS (>~100°C, Ueki and Iwamori 2013). In addition, it has been confirmed that pMELTS matches the melt fraction vs. major element trends observed in the experiments on ultra-depleted DMM1 (Wasylenki et al. 2003). In conjunction with the good reproducibility of the melt fraction vs. residual phase modes (Figs. S1a, S1c and S1e), the use of alphaMELTS here is encouraging and reassuring, although there still has a slight overestimation of temperature.

## 2. Dependence on the parametric models

As mentioned, many investigations have been conducted on the SCSS model (Mavrogenes and O'Neill 1999; Li and Ripley 2005, 2009; Liu et al. 2007; Moretti and Baker 2008; Ariskin et al. 2013; Fortin et al. 2015; Smythe et al. 2017), $D_{Ni}^{Ol/melt}$ (Hart and Davis 1978; Beattie et al. 1991; Li and Ripley 2010; Putirka et al. 2011; Niu et al. 2011; Herzberg et al. 2013, 2016; Matzen et al. 2013, 2017a), $D_{Ni}^{Sul/melt}$ and $D_{Cu}^{Sul/melt}$ (Gaetani and Grove 1997; Ripley et al. 2002; Li and Audétat 2012; Patten et al. 2013; Kiseeva and Wood 2013, 2015), triggering a lively debate on these parametric models that feature prominently in the partitioning behaviors of Ni

and Cu during partial melting. In the manuscript, we used what we considered to be the most suitable parameterizations. Here we further test the differences induced by other choices of parameterizations (e.g., SCSS, $D_{Ni}^{Ol/melt}$ and $D_{Cu}^{Sul/melt}$), using the example of adiabatic decompression melting of primitive mantle with $T_p$=1500°C (Fig. S2).

The S content in melt output is equal to SCSS before the complete exhaustion of residual sulfide, and then, will decrease by dilution as more melt is produced by the S-free residual mantle. The Fortin et al. (2015) model gives the greatest SCSS at low melting fraction, leading to the most rapid depletion of sulfide in the mantle (~6.38 wt.% melting). The calculated SCSS from Li and Ripley (2009) slightly increases at first with increasing melting, then gradually diminishes before the residual sulfide has been exhausted (~9.24 wt.% melting). The picrite model from Mavrogenes and O'Neill (1999) results in a perpetually increasing SCSS before sulfide out (~10.94 wt.% melting). The SCSS parameterization used by the model of Mungall and Brenan (2014) depends on the pressure, temperature, $f_{O_2}$, $a_{FeS}$ and the total Fe (as $Fe_2O_3$) in melt, offering the lowest sulfur concentration trend with a kink point due to the exhaustion of garnet. The recent model by Smythe et al. (2017) incorporates reduction of SCSS due to the effects of Ni and Cu activities in sulfide phase, predicting a monotonic decrease with the increasing degree of melting, which agrees closely to the result of Mungall and Brenan (2014). The various expressions of sulfur trends in Figure S2a can be attributed to the fact that these SCSS models used different experimental databases for calibration and divergent parameters in their empirical equations. However, the influences of various SCSS models on the overall behavior of Ni are negligible (Fig. S2b) because the contribution of the residual sulfide phase to the bulk partition coefficient between the restite and melt is little due to the low concentration of sulfide.

On the other hand, as Ni is dominantly hosted by olivine in the restite, its concentration in the melt is mostly controlled by the partition coefficient between olivine and melt, which depends on melt composition, pressure and temperature (Hart and Davis 1978; Beattie et al. 1991; Wang and Gaetani 2008; Filiberto et al. 2009; Li and Ripley 2010; Putirka et al. 2011; Niu et al. 2011; Herzberg et al. 2013; Matzen et al. 2013, 2017a). Unlike other empirical expressions for $D_{Ni}^{Ol/melt}$, the parameterization of Li and Ripley (2009) shows a higher concentration of Ni along the entire melting path (Fig. S2c), because the sensitivity of this model to the changes in temperature is weaker than other equations (Fig. 1b in Matzen et al. 2013), resulting in a lower $D_{Ni}^{Ol/melt}$ throughout the falling temperature range during decompression melting. In contrast, the Putirka et al. (2011) parameterization gives the lowest Ni in melt at high degrees of melting (Fig. S2c), owing to its large $D_{Ni}^{Ol/melt}$ (Herzberg et al. 2013). The results from Mungall and Brenan (2014) and Herzberg et al. (2013) exhibit the slightly higher Ni amounts at low melting, and are close to (even overlapped with) the trend predicted by the model of Matzen et al. (2017a) at the higher degree of melting (Fig. S2c). It is important to note that the equation from Herzberg et al. (2013) is just a function of MgO content of primary magma, and hence, this result only requires the composition output of alphaMELTS program without additional superimposed calculations, which can be used as an independent check for the accuracy of our models.

Figure S2d shows the influences of different SCSS models on the evolution of Cu in melt using the $D_{Cu}^{sul/melt}$ model from Kiseeva and Wood (2013, 2015); and the results obtained from different assumptions of constant $D_{Cu}^{sul/melt}$ (100, 360, 650 and 1000) were also included. The

SCSS models from Mungall and Brenan (2014), Fortin et al. (2015) and Smythe et al. (2017) resulted in the calculated Cu trends that decrease monotonically with increasing melting whereas the remaining two models exhibit concave-upward trends of Cu concentrations (Fig. S2d). After sulfide exhaustion, these trends overlap because the Cu contents in this stage depend only on the melting fraction and the bulk partition coefficient between the silicate melt and sulfur-free residual mantle. But compared with the various SCSS models, the decrease of $D_{Cu}^{sul/melt}$ from 1000 to 100 leads to a clockwise rotation of the part of Cu trends before sulfide exhaustion, transferring from an inverted 'V' curve to the near-linear negative relationship (Fig. S2d). As a result, for the partitioning behavior of Cu, the influence of $D_{Cu}^{sul/melt}$ prevails over that of different SCSS models, which affect the Cu trends solely by determining when the residual sulfide has been completely dissolved.

## 3. Partitioning models and mass balance equations

The distributions of Ni and Cu between silicate melt and residual mantle can be calculated through two simple alternative mathematical models. One is the equilibrium model, which implies complete equilibration between the restite and melt, and the trace element concentration dissolved in melt ($C_i$) can be calculated based on mass balance:

$$C_i = \frac{C_i^o}{F + (1-F)D_i^{bulk}} \qquad (SE1)$$

where *i* is the element of Ni or Cu, $C_i^0$ is the original concentration of *i* in the melt, $D_i^{bulk}$ is the bulk partition coefficient of *i* between the melt and restite, F is the melt fraction. Another model is the fractional model, in which only the infinitesimally small amount of melt equilibrates with the restite before instantaneous melt extraction, and the trace element concentration within melt can be written as (Shaw 1970):

$$C_i = \frac{C_i^0}{D_i^{bulk}}(1-F)^{\frac{1}{D_i^{bulk}}-1} \qquad (SE2)$$

and the element *i* content of aggregated silicate melt ($C_i'$) is integrated as (Shaw 1970):

$$C_i' = \frac{C_i^0}{F}\left(1-(1-F)^{\frac{1}{D_i^{bulk}}}\right) \qquad (SE3)$$

Furthermore, if the partitioning process is considered in greater detail, in general, the minerals do not be melted in the proportion in which they exist in the restite. Therefore, a realistic melting model requires a new partition coefficient *P*, which is the individual partition coefficient weighted according the proportions in which the mineral phases enter the melt (Shaw 1970; White 2013), and the equation for the trace element concentration of melt ($C_i$) in this non-modal fraction melting can be written as (Shaw 1970):

$$C_i = \frac{C_i^0}{D_i^{bulk}}\left(1-\frac{PF}{D_i^{bulk}}\right)^{\left(\frac{1}{P}-1\right)} \qquad (SE4)$$

Both the equilibrium and fractional models (modal and non-modal) were adopted in the incremental modeling for the polybaric continuous melting of DMM, while the related differences of element concentrations in melt were less than 3 ppm (Fig. S4) because the melt fraction within each decompressed increment (0.01 GPa) is so extremely low that the equations SE1, SE2 and SE3 closely approximate to $\sim C_i^0/D_i^{bulk}$. In contrast, if the Ni and Cu partitioning behaviors are calculated via the bulk melting model, the Ni concentrations of pooled melts obtained from equilibrium partitioning model are larger than that of fractional model at the same melting fraction (Fig. S4a), while the Cu trends follow the exact opposite (Fig. S4b). In this regard, the assumption of average partition coefficient along the decompression path as the $D_i^{bulk}$ in bulk melting model would drive a large systematic error (Fig. S4), especially a downward trend of Cu without the subsequent increase that should be induced by the complete exhaustion of residual sulfide during the partial melting of DMM (shown in Figs. 2d, 3b and S3b). However, the systematic error was largely reduced when the $D_i^{bulk}$ was calculated as the mass-weighted average partition coefficient along the melting path (Fig. S4), in which the "mass" refers to the mass of melted mantle at each increment.

The amount of residual sulfide is calculated based on the mass balance of sulfur between the silicate melt and restite. Before the complete exhaustion of sulfide in source, silicate melt in each increment is S-saturated, and hence the sulfur content of the extracted melt is calculated via the SCSS model. Due to the mass balance equation, we obtain the amount of sulfur remaining in the restite via subtracting the dissolved sulfur in melt from the total amount of sulfur in the proposed mantle. Following the assumption of Naldrett (2011), the sulfide content in restite is 2.75 times larger than its sulfur amount, which is slightly greater than the S proportion of FeS.

In each 0.01GPa increment of decompression melting, once the melt fraction by volume exceeds the fixed threshold, the extra part will be extracted, and the entropy and composition of restite are used as reference for the next increment. The extraction of melt at the *i*-th increment will take some sulfur away from the system, and the sulfur in restite at the next increment (*i+1*) can be calculated as:

$$W_{R_{i+1}} = \left(W_{R_i} m_{R_i} + W_{L_i} m_{L_i} V_0/V_i - W_{L_{i+1}} m_{L_{i+1}}\right)/m_{R_{i+1}} \qquad (SE5)$$

where $m_{R_i}$ and $m_{L_i}$ are the mass of restite and melt at the *i*-th increment, $V_i$ is the volume proportion of melt at *i*-th increment, $V_0$ is the fixed threshold of the volume proportion, $W_{R_i}$ and $W_{L_i}$ are the mass percent (wt.%) of sulfur for residual mantle and melt at the *i*-th increment. In next increment, the subscripts within these parameters are replaced with *i+1*.

When the sulfur amount in the system at *n*-th increment cannot provide enough sulfur for achieving the S solubility of melt in the next increment ($\left(W_{R_n} m_{R_n} + W_{L_n} m_{L_n} V_0/V_n\right) < W_{L_{n+1}} m_{L_{n+1}}$), the sulfide will be completely exhausted at the (*n+1*)-th increment. In this condition, the sulfur content of melt will be unequal to its solubility ($W_{L_{n+1}} \neq S_{L_{n+1}}$), and can be calculated as:

$$W_{L_{n+1}} = \frac{W_{R_n} m_{R_n} + \dfrac{W_{L_n} m_{L_n} V_0}{V_n}}{m_{L_{n+1}}} \qquad (SE6)$$

After the exhaustion of residual sulfide, the amount of sulfur in melt will be diluted continuously due to the subsequent generation and extraction of melts, and can be estimated by the following equation:

$$W_{L_{i+1}} = \frac{W_{L_i} m_{L_i} V_0}{m_{L_{i+1}} V_i} (here, i \geq n+1) \qquad (SE7)$$

Therefore, the sulfur amounts of residual mantle and silicate melt at each increment can be worked out during the polybaric continuous melting of DMM. On the other hand, the concentrations of S, Ni, and Cu in the magma output are calculated from the integration of their contents in the extracted melt at each increment by the following equation (Asimow et al. 2001):

$$\acute{C} = \frac{\int_{P_0}^{P_f} C_i F_i dP}{\int_{P_0}^{P_f} F_i dP} \qquad (SE8)$$

where $\acute{C}$ is the calculated concentration in the magma output, $C_i$ and $F_i$ are the amount of elements and fraction of extracted melt at the *i*-th increment, respectively, $P_0$ is the initial pressure of melting and $P_f$ is final pressure of melting.

## 4. Different melting mechanisms

In order to evaluate the influences of fractional melting, continuous melting and adiabatic melting on the melt composition during decompression, a comparison between them is shown in Figure S5. As melt productivity is low at the initial melting stage (Fig. S5a), the pressure and/or temperature effect dominates. Therefore, the decrease of MgO induced by pressure drop is manifested most strongly at low melting degree, showing a steep negative slope in Figure S5b. Once garnet in the source is exhausted, these models show a sharp increase in melt productivity. For fractional melting, melt productivity increases smoothly, and exhibits a rapid growth just before the exhaustion of clinopyroxene (Fig. S5b), followed by a large drop (~10 %/GPa). As a result, the aggregated melt in fractional melting is mostly generated over a narrow range of pressure just before the exhaustion of clinopyroxene, and pressure drop in this stage has little effect on the MgO of melt, corresponding to less than 3% decrease of MgO in magmatic products. As a result, the complex magma composition produced by fractional melting can be roughly represented and constrained by an appropriate isobaric melting model (Herzberg and O`Hara 2002). On the other hand, the melt productivity of adiabatic melting continuously increases between the exhaustion of garnet and clinopyroxene, and is larger than that of fractional melting at the same pressure. Thus, the exhaustion of clinopyroxene during adiabatic melting occurs at a slightly higher pressure (Fig. S5a), and the melt output comes from the persistent contributions of the entire upwelling process, rather than a narrow range with high melt productivity before the exhaustion of clinopyroxene. Hence, the influence of pressure variation on the melt composition is enhanced in the adiabatic melting model, resulting in a larger decrease of MgO than the fractional melting at the same pressure drop (Fig. S5b). Before the exhaustion of orthopyroxene, the melt productivity of adiabatic melting still increases, but its value is lower than that stage before clinopyroxene exhaustion, which coincides with the smooth negative slope of MgO in Figure S5b. After orthopyroxene-out, its melt productivity comes down to a low level, and olivine becomes the main phase to be dissolved leading to the extreme

final increase of MgO in melt. Melt productivity for continuous melting should be zero before the melt fraction by volume exceeds the fixed threshold (Fig. S5b). Then, the variation of its melt productivity is quite similar to that of fractional melting, corresponding to the parallel trends of MgO in aggregated melts (Fig. S5b). Among these models, the difference between their temperatures is less than 1℃at the same pressure, and hence, the various trends of MgO in melt are attributed to their different melt productivities during the decompression process, which will be also reflected in the variations of Ni during melting (Fig. S5c). In contrast, as the partition coefficients of Cu between mineral phases and melt are assumed as constants, the influences of melt productivity in fractional, adiabatic and continuous melting are slight, being embodied only in the exhaustion of sulfide (Fig. S5d), if we do not consider the buffering of remaining melt.

In all, the different trends of Ni in the isobaric and decompression melting are mostly controlled by the variations of $D_{Ni}^{Ol/melt}$. For decompression melting, the slow decrease of temperature and quick drop of pressure will decrease the MgO in melt; all of these factors trigger an increase of $D_{Ni}^{Ol/melt}$ and the associated reduction of Ni in melt. The differences of melt productivity in these melting mechanisms (fractional, adiabatic and continuous) will cause slight variations on the MgO, Ni and Cu behaviors, but do not modify the broad picture of their distribution during mantle melting.

## 5. Olivine-sulfide equilibria

The equilibrium distribution coefficient for the exchange of Fe and Ni between coexisting olivine and sulfide liquid ($K_d = (X_{NiS}/X_{FeS})_{sulfide}/(X_{NiO}/X_{FeO})_{olivine}$, $X_i$ = mole fraction) during mantle melting can be calculated through the compositions of modeled compositions of olivine and BMS. Additionally, many experimental measurements of this parameter have been conducted at controlled pressure, oxygen and sulfur fugacities (1-atm, log $f_{O_2}$=-7.6 to -10.6, log $f_{S_2}$=-0.9 to -2.5) over the temperature range of ~ 1200-1385℃, with different sulfide liquid compositions (5-58 wt.% Ni, 7-18 wt.% Cu) (Fleet and MacRae 1983, 1987, 1988; Gaetani and Grove 1997; Brenan and Caciagli 2000; Brenan 2003). Because the effects of pressure on $D_{Ni}^{ol/melt}$ and $D_{Ni}^{sul/melt}$ are subordinate within the range from 0-3 GPa (Kiseeva and Wood 2013, 2015; Matzen et al. 2013, 2017a), we should expect that the $K_d$ derived from our models should be consistent with the published experimental data, which, more recently, has been expressed as parameterizations (e.g., Barnes et al. 2013; Sciortino et al. 2015; Mao et al., 2017). These parameterizations were hampered by the existence of contradictory results in the experimental database at high values of $K_d$. It has been widely proposed that the $K_d$ depends on multiple independent variables: temperature, sulfide composition, $f_{O_2}$ and $f_{S_2}$, and that $K_d$ decreases with increasing temperature at constant $f_{O_2}$ relative to the FMQ buffer (Brenan 2003). In our model, besides temperature, variation of sulfide composition was also taken into account within the $D_{Ni}^{sul/melt}$ (Kiseeva and Wood 2015), and the influences of oxygen and sulphur fugacities were simplified by treating Ni partitioning in terms of an exchange reaction between NiO in silicate melt and FeS in sulfide liquid (Kiseeva and Wood 2013). Hence, the potential controlling factors in experiments all affected the values of $K_d$ that emerged from our calculations despite the fact that we did not explicitly determine a value for $K_d$ itself. The projected curves for $K_d$ versus Ni wt.% of BMS are plotted for the polybaric continuous melting of DMM (Fig. S7a) and isobaric melting of SCLM (Fig. S7b) at ΔFMQ-1. Within the appropriate range (temperature, 1300 to

1400℃; log$f_{O_2}$, -7.32 to -8.25) where there are sufficient experimental data, our predicted trends of $K_d$ are broadly consistent with previous parameterizations (Figs. S7a and S7b), but differ dramatically from them over the wider range of conditions addressed by our models. The estimated $K_d$ that emerges from our model, based on completely independent considerations of the compositions of olivine and sulfide, is far closer to observed values in natural peridotites (Fig. S7c). Hence, the partitioning behaviors of Ni predicted for equilibration of olivine-silicate melt (Matzen et al. 2013, 2017a), sulfide melt-silicate melt (Kiseeva and Wood 2013, 2015) and olivine-sulfide melt (Brenan and Caciagli 2000; Brenan 2003) are self-consistent in our models, but the accuracy of previously published $K_d$ parameterizations at extended ranges of temperature and $f_{O_2}$ is poor due to the lack of a self-consistent experimental database and the complex interplay among the temperature, $f_{O_2}$ and $f_{S_2}$.

The $K_d$ has been widely used as a petrogenetic indicator for the olivine-BMS equilibria which, in turn, suggests the occurrence of later-magmatic, secondary processes, e.g., metasomatism, segregation, refertilization and desulphurization, if this equilibrium has not been reached (Fleet and Stone 1990; Szabó and Bodnar 1995; Shaw 1997; Ishimaru and Arai 2008; Lorand and Grégoire 2006; Galán et al. 2016). The experimental $K_d$ has long been considered to be rather constant (31, Brenan 2003; 28-35, Fleet 2001) over a wide range of Ni concentrations in BMS, whereas most natural peridotite xenoliths in the literature fall into a lower range of $K_d$ (~8-20, Fleet and Stone 1990; Szabó and Bodnar 1995; Shaw 1997; Lorand and Grégoire 2006; Ishimaru and Arai 2008). However, the $K_d$ predicted by our model exhibits a positive trend with extent of decompression melting of mantle (Fig. S7a) or decreasing trend in isobaric melting of SCLM (Fig. S7b) due to the simultaneous variations of multiple independent variables. Our models are in good agreement with the variations of $K_d$ from Hannuoba peridotites, North China Craton, whose highly siderophile element patterns are considered to demonstrate melt depletion and long-term preservation of sulfides (Liu et al. 2010). The sulfide-melt inclusions within lherzolite xenoliths from Changbaishan district (Xu and Xie 2007), and protogranular xenoliths from Nógrád-Gömör Volcanic Field (Szabó and Bodnar 1995), are also matched by our partial melting trends, but additional evidence is needed to confirm the residual origin of these BMS. Although the compositions of Yangyuan peridotites are similar to or slightly more depleted than Hannuoba xenoliths, the lower $K_d$ and Ni wt. % within sulfide-melt inclusions may come from sulfide breakdown that occurred during interaction with a S-undersaturated melt or fluid (Liu et al. 2010). Additionally, within the West Eifel xenoliths, the sulfides formed from metasomatic events of mantle also fall into a range similar to the Yangyuan peridotites (Shaw 1997). However, these variations of BMS are not only generated from the metasomatism of mantle, e.g., most sulfides within Kaapvaal peridotites display main characteristics of residual origin (Griffin et al. 2004), but still have analogous low-values of $K_d$ and Ni wt. % (Lorand and Grégoire 2006, Fig. S7c). Considering the broad distribution of data for sulfide-melt inclusions from distinct xenoliths (Fig. S7c) and the potential occurrences of multiple secondary processes for BMS, we concur with the previous conclusion that the $K_d$ may just provide auxiliary, non-critical evidence for the origin of BMS in mantle xenoliths (Lorand and Grégoire 2006). The long-hold views of near-constant equilibrium value of $K_d$ under conditions in the upper mantle based largely on attempts to parameterize the experimental data set appear to be unjustified, being inconsistent both with observed mineral compositions and with the predictions of the best currently available estimates of olivine-sulfide melt-silicate melt Ni partitioning.

## 6. Correction for fractionation effect

It has been confirmed that most OIBs and MORBs compositions are not primary melts, but are various evolved derivatives, primarily through the fractional crystallization during the cooling at shallow levels (Langmuir 1989; Niu and O'Hara 2008). Therefore, in order to depict the mantle signals from OIBs, correction for the effect of crustal-level fractionation crystallization is required. Because of the abundant compositional data and research methods of mid-ocean ridge basalts, the MORB glasses worldwide offer an unrivalled opportunity to do the fractionation correction (Niu et al. 1999). We follow the approach of Niu et al. (1999) and Niu and O'Hara (2008) and use polynomial fitting to correct for the olivine fractionation to $Mg^{\#}$=0.72 ($Mg^{\#}$= Mg/(Mg+$Fe^{2+}$), assuming 90% of total Fe as $Fe^{2+}$ in natural MORB glasses. More than 17000 glass analyses of MORB are available in the global database (PetDB, http://www.petdb.org/). In this work, we excluded samples (1) with $SiO_2$>53 wt.% to ensure minimal crustal level modification; (2) with MgO<7 wt.% to avoid unnecessary errors relating to fractionation correction for the more evolved samples; (3) without the accurate concentrations of Ni and Cu, leaving 2596 samples on a global scale to work with. Based on these samples, the polynomial equation for Ni is

$$Ni(wt.\%) = 1.8273 - 27.205Mg^{\#} + 150.25\left(Mg^{\#}\right)^2 - 409.95\left(Mg^{\#}\right)^3 + 595.2(Mg^{\#})^4 - 441.25(Mg^{\#})^5 + 131.57(Mg^{\#})^6 \quad R^2 = 0.4168 \qquad (SE8)$$

Using this relationship, we move all data points back along the liquid line of descent (LLD) to $Mg^{\#}$=0.72. Although individual MORB suites ideally should be corrected using unique sets of correction coefficients as shown for the East Pacific Rise (Niu et al. 1999), the single set of correction coefficients here is adequate to reveal the first-order compositional systematics of the global MORBs and OIBs (Klein and Langmuir 1987; Niu and O'Hara 2008; Humphreys and Niu 2009).

## References cited

Ariskin, A.A., Danyushevsky, L.V., Bychkov, K.A., McNeill, A.W., Barmina, G.S., and Nikolaev, G.S. (2013) Modeling solubility of Fe-Ni sulfide in basaltic magmas: the effect of nickel. Economic Geology 108, 1983-2003.

Asimow, P.D., Hirschmann, M.M., and Stolper, E.M. (2001) Calculation of peridotite partial melting from thermodynamic models of minerals and melts, IV. adiabatic decompression and the composition and mean properties of Mid-ocean Ridge Basalts. Journal of Petrology, 42, 963-998.

Asimow, P.D., Dixon, J.E., and Langmuir, C.H. (2004) A hydrous melting and fractionation model for mid-ocean ridge basalts: application to the Mid-Atlantic Ridge near the Azores. Geochemistry, Geophysics, Geosystems, 5. Doi:10.1029/2003GC000568

Baker, M.B., and Stolper, E.M. (1994) Determining the composition of high-pressure mantle melts using diamond aggregates. Geochimica et Cosmochimica Acta, 58, 2811-2827.

Baker, M.B., Hirschmann, M.M., Ghiorso, M.S., and Stolper, E.M. (1995) Compositions of near-solidus peridotite melts from experiments and thermodynamic calculations. Nature, 375, 308-311.

Barnes, S.J., Godel, B., Gürer, D., Brenan, J.M., Robertson, J., and Paterson D. (2013) Sulfide-olivine Fe-Ni exchange and the origin of anomalougly Ni rich magmatic sulfides. Economic Geology, 108, 1971-1982.

Beattie, P., Ford, C., and Russell, D. (1991) Partition coefficients for olivine-melt and orthopyroxene-melt systems. Contributions to Mineralogy and Petrology, 109, 212-224.

Brenan, J.M. (2003) Effects of $fO_2$, $fS_2$, temperature, and melt composition on Fe-Ni exchange between olivine and sulfide liquid: Implications fro natural olivine-sulfide assemblages. Geochimica et Cosmochimica Acta, 67, 2663-2681.

Brenan, J.M., and Caciagli, N.C. (2000) Fe-Ni exchange between olivine and sulfide liquid: Implications for oxygen barometry. Geochimica et Cosmochimica Acta, 64, 307-320.

Connolly, J.A.D. (2005) Computation of phase equilibria by linear programming: a tool for geodynamic modeling and its application to subduction zone decarbonation. Earth and Planetary Science Letters, 236, 524-541.

Falloon, T.J., Green, D.H., Danyushevsky, L.V., and Faul, U.H. (1999) Peridotite melting at 1.0 and 1.5 GPa: an experimental evaluation of techniques using diamond aggregates and mineral mixes for determination of near-solidus melts. Journal of Petrology, 40, 1343-1375.

Falloon, T.J., Danyushevsky, L.V., and Green, D.H. (2001) Peridotite melting at 1 GPa: reversal experiments on partial melt compositions produced by peridotite-basalt sandwich experiments. Journal of Petrology, 42, 2363-2390.

Falloon, T.J., Green, D.H., Danyushevsky, L.V., and McNeill, A.W. (2008) The composition of near-solidus partial melts of fertile peridotite at 1 and 1.5 GPa: implications for the petrogenesis of MORB. Journal of Petrology, 49, 591-613.

Filiberto, J., Jackson, C., Le, L., and Treiman, A.H. (2009) Partitioning of Ni between olivine and an iron-rich basalt: experiments, partition models, and planetary implications. American Mineralogist, 94, 256-261.

Fleet, M.E. (2001) A comment of "Fe-Ni exchange between olivine and sulphide liquid: Implications for oxygen barometry in sulphide-saturated magmas" by Brenan and Caciagli (2000). Geochimica et Cosmochimica Acta, 65, 4425-4427.

Fleet, M.E., and MacRae, N.D. (1983) Partition of Ni between olivine and sulfide and its application to Ni-Cu sulfide deposits. Contributions to Mineralogy and Petrology, 83, 75-81.

Fleet, M.E., and MacRae, N.D. (1987) Partition of Ni between olivine and sulfide: the effect of temperature, $fO_2$ and $fS_2$. Contributions to Mineralogy and Petrology, 85, 336-342.

Fleet, M.E., and MacRae, N.D. (1988) Partition of Ni between olivine and sulfide: Equilibriia with sulfide-oxide liquid. Contributions to Mineralogy and Petrology, 100, 462-469.

Fleet, M.E., and Stone W.E. (1990) Nickeliferous sulfides in xenoliths, olivine megacrysts and basaltic glass. Contributions to Mineralogy and Petrology, 105, 629-636.

Fortin, M. A., Riddle, J., Desjardins-Langlais, Y., Baker, D. R., (2015). The effect of water on the sulfur concentration at sulfide saturation (SCSS) in natural melts. Geochimica et Cosmochimica Acta, 100-116.

Galán, G., Cruz, E., Fernández-Roig, M., Martínez, F.J., and Oliveras V. (2016) Mineral associations and major element compositions of base metal sulphides from the subcontinental lithospheric mantle of NE Spain. Mineralogy and Petrology, 110, 87-101.

Gaetani, G.A., and Grove, T.L. (1997) Partitioning of moderately siderophile elements among olivine, silicate melt, and sulfide melt: constraints on core formation in the Earth and Mars. Geochimica et Cosmochimica Acta, 61, 1829-1846.

Ghiorso, M., (1994) Algorithms for the estimation of phase-stability in heterogeneous thermodynamic systems. Geochimica et Cosmochimica Acta, 58, 5489-5501.

Ghiorso, M., and Sack, R. (1995) Chemical mass transfer in magmatic processes. IV. A revised and internally consistent thermodynamic model for the interpolation and extrapolation of liquid-solid equilibria in magmatic systems at elevated temperatures and pressure. Contributions to Mineralogy and Petrology, 119, 197-212.

Ghiorso, M.S., Hirschmann, M.M., Reiners, P.W., and Kress, V.C. (2002) The pMELTS: A revision of MELTS for improved calculation of phase relation and major element partitioning related to partial melting of the mantle to 3 GPa. Geochemistry, Geophysics, Geosystems, 3. Doi:10.1029/2002GC000217

Griffin, W.L., Graham, S., O'Reilly, S.Y., and Pearson N.J. (2004) Lithosphere evolution beneath the Kaapvaal Craton: Re-Os systematics of sulfides in mantle-derived peridotites. Chemical Geology, 208, 89-118.

Grove, T.L., Holbig, E.S., Barr, J.A., Till, C.B., and Krawczynski, M.J. (2013) Melts of garnet lherzolite: experiments, models and comparison to melts of pyroxenite ad carbonated lherzolite. Contribuions to Mineralogy and Petrology, 166, 887-910.

Hart, S.R., and Davis, K.E. (1978) Nickel partitionging between olivine and silicate melt. Earth and Planetary Science Letters, 40, 203-219.

Herzberg, C., and O'Hara, M.J. (2002) Plume-associated ultramafic magmas of Phanerozoic age. Journal of Petrology, 43, 1857-1883.

Herzberg, C., Asimow, P.D., Ionov, D.A., Vidito, C., Jackson, M.G., and Geist, D. (2013) Nickel and helium evidence for melt above the core-mantle boundary. Nature, 493, 393-398.

Herzberg, C., Vidito, C., and Starkey, N.A. (2016) Nickel-cobalt contents of olivine record origins of mantle peridotite and related rocks. American Mineralogist, 101, 1952-1966.

Holland, T.J.B., and Powell, R. (2011) An improved and extended internally-consistent thermodynamic dataset for phases of petrological interest, involving a new equation of state for solids. Journal of Metamorphic Geology, 29, 333-383.

Humphreys, E.R., and Niu, Y. (2009) On the composition of ocean island basalts (OIB): the effects of lithospheric thickness variation and mantle metasomatism. Lithos, 112, 118-136.

Ishimaru, S., and Arai, S. (2008) Nickel enrichment in mantle olivine beneath a volcanic front. Contributions to Mineralogy and Petrology, 156, 119-131.

Jennings, E.S., and Holland, T.J.B. (2015) A simple thermodynamic model for melting of peridotite in the system NCFMASOCr. Journal of Petrology, 56, 869-892.

Katz, R.F., Spiegelman, M., and Langmuir, C. H. (2003) A new parameterization of hydrous mantle melting. Geochemistry, Geophysics, Geosystems, 4. Doi:10.1029/2002GC000433

Kimura, J.I., van Keken, P., Hacker, B.R., Kawabata, H., Yoshida, T., and Stern, R.J. (2009) Arc basalt simulator (ABS) version 2, a simulation model for slab dehydration, fluid-mantle reaction, and fluid-fluxed mantle melting for arc basalts: modeling scheme and application. Geochemistry, Geophysics, Geosystems, 7. Doi:10.1029/2008GC002217

Kimura, J.I., Adam, J.R.K., Rowe, M., Nakano, N., Katakuse, M., van Keken, P., Hacker, B., and Stern, R.J. (2010) Origin of cross-chain geochemical variation in Quaternary lavas from northern Izu arc: a quantitative mass balance approach on source identification and mantle wedge processes. Geochemistry, Geophysics, Geosystems, 11. Doi:10.1029/2010GC003050

Kimura, J.I., and Kawabata, H. (2014) Trace element mass balance in hydrous adiabatic mantle melting: the hydrous adiabatic mantle melting simulator version 1 (HAMMS1). Geochemistry, Geophysics, Geosystems, 15, 2467-2493.

Kinzler, R., and Grove, T. (1992) Primary magmas of midocean ridge basalts: 1. Experiments and methods. Journal of Geophysical Research, 97, 6885-6906.

Kiseeva, E.S., and Wood, B.J. (2013) A simple model for chalcophile element partitioning between sulphide and silicate liquids with geochemical applications. Earth and Planetary Science Letters, 383, 68-81.

Kiseeva, E.S., and Wood, B.J. (2015) The effects of composition and temperature on chalcophile and lithophile element partitioning into magmatic sulphides. Earth and Planetary Science Letters, 424, 280-294.

Klein, E.M., and Langmuir, C.H. (1987) Global correlations of ocean ridge basalt chemistry with axial depth and crustal thickness. Journal of Geophysical Research: Solid Earth, 92. doi:10.1029/JB092iB08p08089

Langmuir, C.H. (1989) Geochemical consequences of in situ crystallization. Nature, 340, 199-205.

Langmuir, C., Klein, E., and Plank, T. (1992) Petrological systematics of mid-oceanic ridge basalts: constraints on melt generation beneath ocean ridges. In J. Phipps, D. Morgan, and J. Sinton, Mantle flow and melt generation at Mid-Ocean Ridges, Geophysical Monograph, 71, Washington, D. C., 183-280.

Li, C., and Ripley, E. M. (2005). Empirical equations to predict the sulfur content of mafic magmas at sulfide saturation and applications to magmatic sulfide deposits. Mineralium Dpeosita, 40, 218-230.

Li, C., and Ripley, E.M. (2009) Sulfur contents at sulfide-liquid or anhydrite saturation in silicate melts: empirical equations and example applications. Economic Geology, 104, 405-412.

Li, C., and Ripley, E.M. (2010) The relative effects of composition and temperature on olivine-liquid Ni partitioning: Statistical deconvolution and implications for petrologic modeling. Chemical Geology, 275, 99-104.

Liu, J., Rudnick, R.L., Walker, R.J., Gao, S., Wu, F.Y., and Piccoli, P.M. (2010) Processes controlling highly siderophile element fractionations in xenolithic peridotites and their influence on Os isotopes. Earth and Planetary Science Letters, 297, 287-297.

Liu, Y., Samaha, N.T., and Baker, D.R. (2007) Sulfur concentration at sulfide saturation (SCSS) in magmatic silicate melts. Geochimica et Cosmochimica Acta, 71, 1783-1799.

Lorand, J.P., and Grégoire M. (2006) Petrogenesis of base metal sulphide assemblages of some peridotites from the Kaapvaal craton (South Africa). Contributions to Mineralogy and Petrology, 151, 521-538.

Mao, Y.J., Qin, K.Z., Barnes, S.J., Ferraina, C., Iacono-Marziano, G., Verrall, M., Tang, D.M., Xue, S.C., (2017). A revised oxygen barometry in sulfide-saturated magmas and application to the Permian magmatic Ni-Cu deposits in the southern Central Asian Orogenic Belt. Mineralium Deposita, doi:10.1007/s00126-017-0771-3

Matzen, A.K., Baker, M.B., Beckett, J.R., and Stolper, E.M. (2013) The temperature and pressure dependence of nickel partitioning between olivine and silicate melt. Journal of Petrology, 54, 2521-2545.

Matzen, A.K., Baker, M.B., Beckett, J.R., Wood, B.J., and Stolper, E.M. (2017a) The effect of liquid composition on the partitioning of Ni between olivine and silicate melt. Contributions to Mineralogy and Petrology, 172, 3. doi:10.1007/s00410-016-1319-8

Mavrogenes, J., and O'Neil, H.S.C. (1999) The relative effects of pressure, temperature and oxygen fugacity on the solubility of sulfide in mafic magmas. Geochimica et Cosmochimica Acta, 63, 1173-1180.

McKenzie, D., and Bickle, M. (1988) The volume and composition of melt generated by extension of the lithosphere. Journal of Petrology, 29, 625-679.

Moretti, R., and Baker, D.R. (2008) Modeling the interplay of $fO_2$ and $fS_2$ along the FeS-silicate melt equilibrium. Chemical Geology, 256, 286-298.

Mungall, J.E., and Brenan, J.M. (2014) Partitioning of platinum-group elements and Au between sulfide liquid and basalt and the origins of mantle-crust fractionation of the chalcophile elements. Geochimica et Cosmochimica Acta, 125, 265-289.

Naldrett, A.J. (2011) Fundamentals of magmatic sulfide deposits. In C. Li, and E.M. Ripley, Ed., Magmatic Ni-Cu and PGE deposits: geology, geochemistry and genesis: reviews in economic geology, volume 17. Society of Economic Geologists, Denver., 1-50.

Niu, Y., and O'Hara, M.J. (2008) Global correlations of ocean ridge basalt chemistry with axial depth: a new perspective. Journal of Petrology, 49, 633-664.

Niu, Y., Collerson, K.D., Batiza, R., Wendt, J.I., and Regelous, M. (1999) Origin of enriched-type mid-ocean ridge basalt at ridges far from mantle plumes: the East Pacific Rise at 11°20′N. Journal of Geophysical Research: Solid Earth, 104, 7067-7087.

Niu, Y., Wilson, M., Humphreys, E.R., and O'Hara, M.J. (2011) The origin of intra-plate ocean island basalts (OIB): the lid effect and its geodynamic implications. Journal of Petrology, 52, 1443-1468.

Patten, C., Barnes, S.J., Mathez, E.A., and Jenner, F.E. (2013) Partition coefficients of chalcophile elements between sulfide and silicate melts and the early crystallization history of sulfide liquid: LA-ICP-MS analysis of MORB sulfide droplets. Chemical Geology, 358, 170-188.

Powell, R., Holland, T., and Worley, B. (1998) Calculating phase diagrams involving solid solutions via non-linear equations, with examples using THERMOCALC. Journal of Metamorphic Geology, 16, 577-588.

Putirka, K.D., Ryerson, F.J., Perfit, M., and Ridley, W.I. (2011) Mineralogy and composition of oceanic mantle. Journal of Petrology, 52, 279-313.

Ripley, E.M., Brophy, J.G., and Li, C. (2002) Copper solubility in a basaltic melt and sulfide liquid/silicate melt partition coefficients of Cu and Fe. Geochimica et Cosmochimica Acta, 125, 265-289.

Sciortino, M., Mungall, J.E., and Muinonen J. (2015) Generation of high-Ni sulfide and alloy phases during serpentinzation of dunite in the Dumont Sill, Quebec. Economic Geology, 110, 733-761.

Shaw, C.S.J. (1997) Origin of sulfide blebs in variably metasomatized mantle xenoliths, Quateranary West Eifel Volcanic Field, Germany. The Canadian Mineralogist, 35, 1453-1463.

Shaw, D.M. (1970) Trace element fractionation during anatexis. Geochimica et Cosmochimica Acta, 34, 237-243.

Smith, P.M., and Asimow, P.D. (2005) Adiabat_1ph: a new public front-end to the MELTS, pMELTS, and pHMELTS models. Geochemistry, Geophysics, Geosystems, 6. Doi:10.1029/2004GC000816

Smythe, D.J., Wood, B.J., and Kiseeva, E.S. (2017) The S content of silicate melts at sulfide saturation: New experiments and a model incorporating the effects of sulfide composition. American Mineralogist, 102, 795-803.

Szabó, C., and Bodnar, R.J. (1995) Chemistry and origin of mantle sulfides in spinel peridotite xenoliths from alkaline basaltic lavas, Nógrád-Gömör Volcanic Field, northern Hungary and southern Slovakia. Geochimica et Cosmochimica Acta, 59, 3917-3927.

Till, C.B., Grove, T.L., and Krawczynski, M.J. (2012) A melting model for variably depleted and enriched lherzolite in the plagioclase and spinel stability fields. Journal of Geophysical Research, 117. Doi:10.1029/2011JB009044

Ueki, K., and Iwamori, H. (2013) Thermodynamic model for partial melting of peridotite by system energy minimization. Geochemistry, Geophysics, Geosystems, 14. Doi:10.1029/2012GC004143

Wang, Z., and Gaetani, G.A. (2008) Partitioning of Ni between olivine and siliceous eclogite partial melt: experimental constraints on the mantle source of Hawaiian basalts. Contributions to Mineralogy and Petrology, 156, 661-678.

Wasylenki, L.E., Baker, M.B., Kent, A.J.R., and Stolper, E.M. (2003) Near-solidus melting of the shallow upper mantle: partial melting experiments on depleted peridotite. Journal of Petrology, 44, 1163-1191.

Xu, J.H., and Xie, Y.L. (2007) Sulfide-melt inclusions in mantle xenoliths from the Changbaishan district, Jilin province, China. Acta Petrologica Sinica, 23, 117-124.

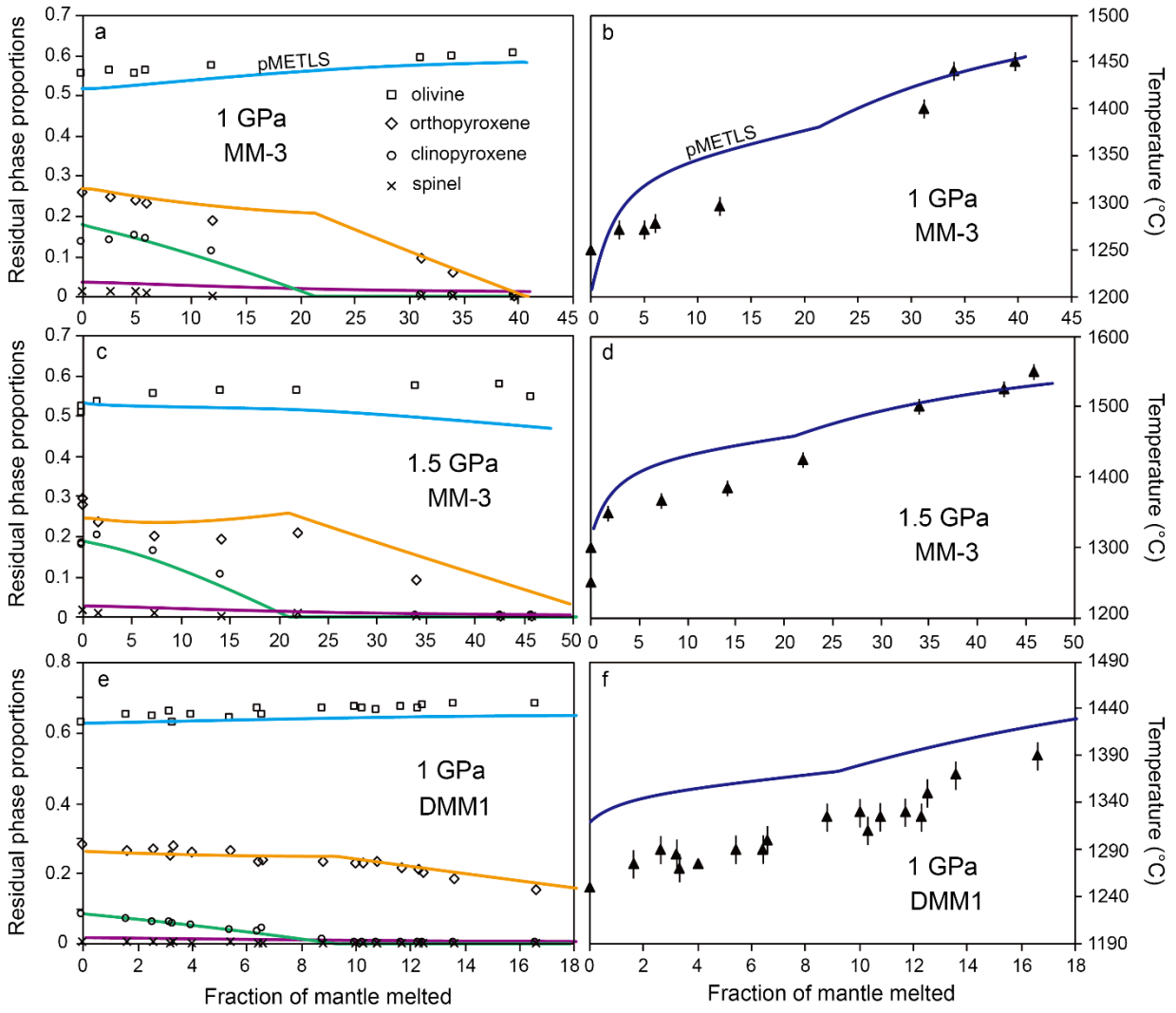


**Figure S1.** Calculated residual phase proportions and temperatures via alphaMELTS for melting of (**a, b**) MM-3 at 1 GPa, (**c, d**) MM-3 at 1.5 GPa, (**e, f**) DMM1 at 1 GPa compared between the experimental results of Falloon et al. (2001, 2008) for MM3, and Wasylenki et al. (2003) for DMM1. Calculated phase proportions and temperatures are shown by colored lines, with experimental results shown by different symbols for specific mineral phases. Temperature uncertainties are ±15°C for the DMM1 experiments and ±10°C for the MM3 experiments.

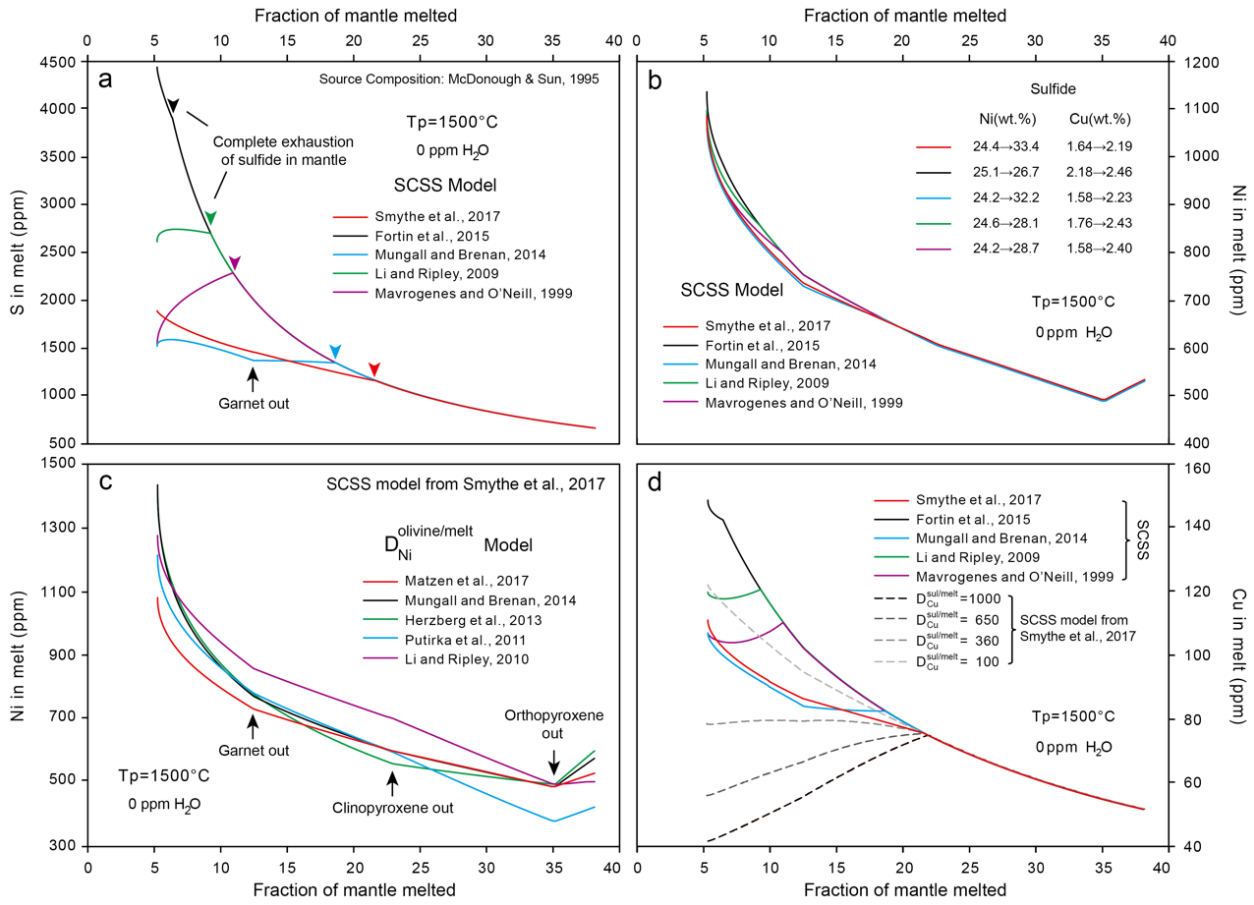


**Figure S2.** The controls of various SCSS models on the evolution of (**a**) sulfur and (**b**) Ni during adiabatic decompression melting of PM at 1500℃ $T_p$ and anhydrous condition. Moreover, the influences of different $D^{Ol/melt}$ and $D_{Cu}^{sul/melt}$ on the behaviors of Ni and Cu concentrations in melt were exhibited in (**c**) and (**d**).

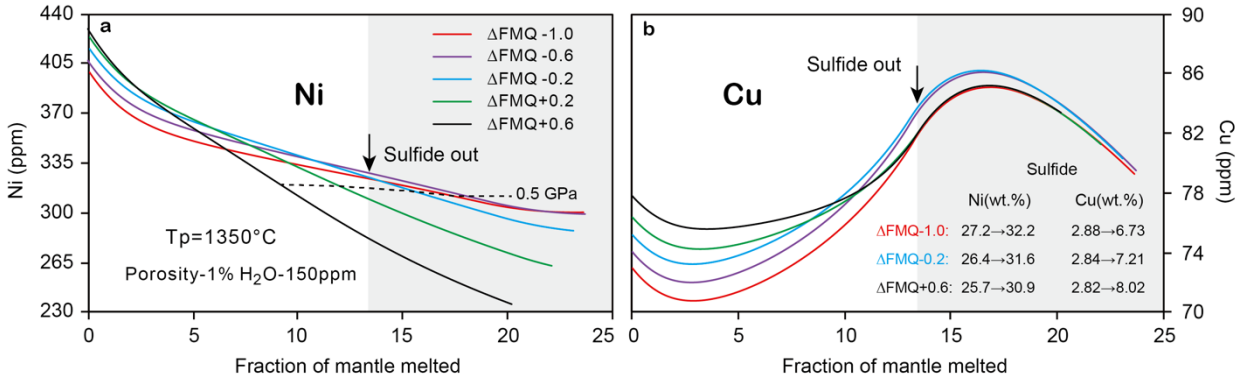


**Figure S3**. Variations of (**a**) Ni and (**b**) Cu concentrations of pooled melt during the polybaric continuous melting of DMM with 1350℃ $T_p$, 150 ppm $H_2O$ and 1.0 vol.% remaining melt under the fixed oxygen fugacity (ΔFMQ -1.0, -0.6, -0.2, +0.2 and +0.6). The dash line in (**a**) means the constant pressure value, 0.5 GPa. The grey vertical bands in (**a**-**b**) indicate the reference area in which the residual sulfide has been completely dissolved.

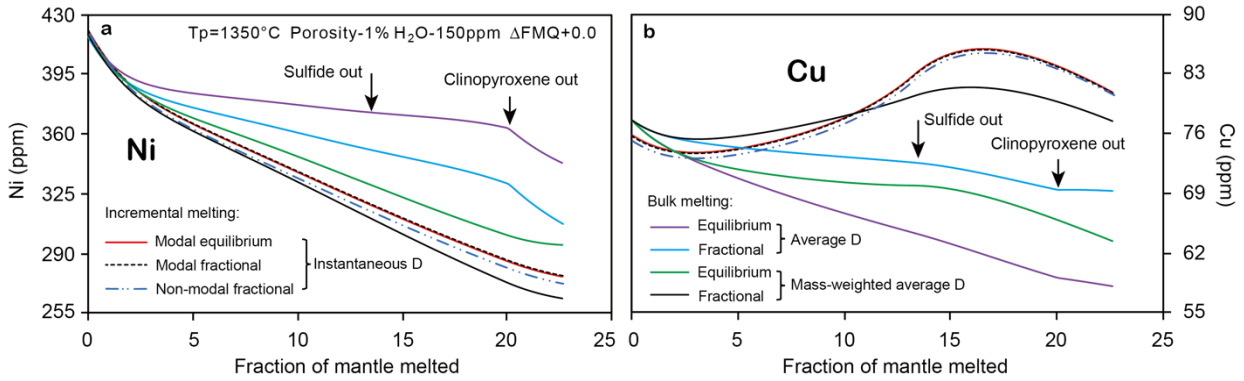


**Figure S4**. Variations of (**a**) Ni and (**b**) Cu concentrations of pooled melt during the polybaric continuous melting of DMM with 1350℃ $T_p$, 150 ppm $H_2O$, 1.0 vol.% remaining melt and ΔFMQ +0.0 under different models of the partition coefficients. See details in the Supplement 3.

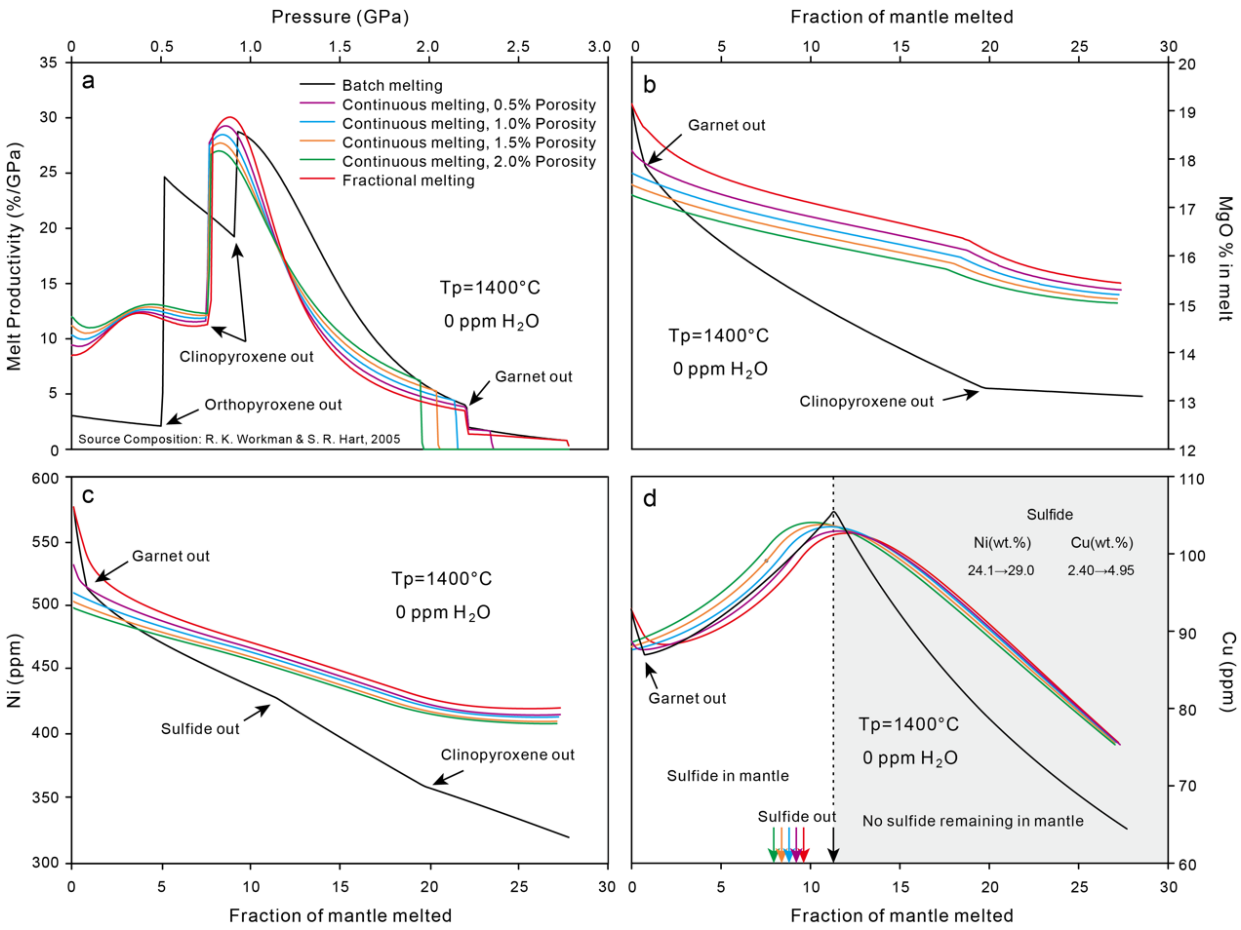


**Figure S5.** Variations of (**a**) melt productivity, (**b**) MgO, (**c**) Ni and (**d**) Cu concentrations of melt during the decompression melting of DMM with 1400℃ $T_p$ and 0 ppm $H_2O$. Adiabatic, fractional and continuous melting (0.5, 1.0, 1.5 and 2.0 vol. % remaining melt) models were conducted to exhibit the effect of different mechanisms of partial melting on these parameters in magma products. The colored arrows in (**d**) indicate the complete exhaustion of sulfide in mantle for different mechanisms. The gray vertical band in (**d**) indicates the reference area in which the residual sulfide has been completely dissolved for the adiabatic melting.

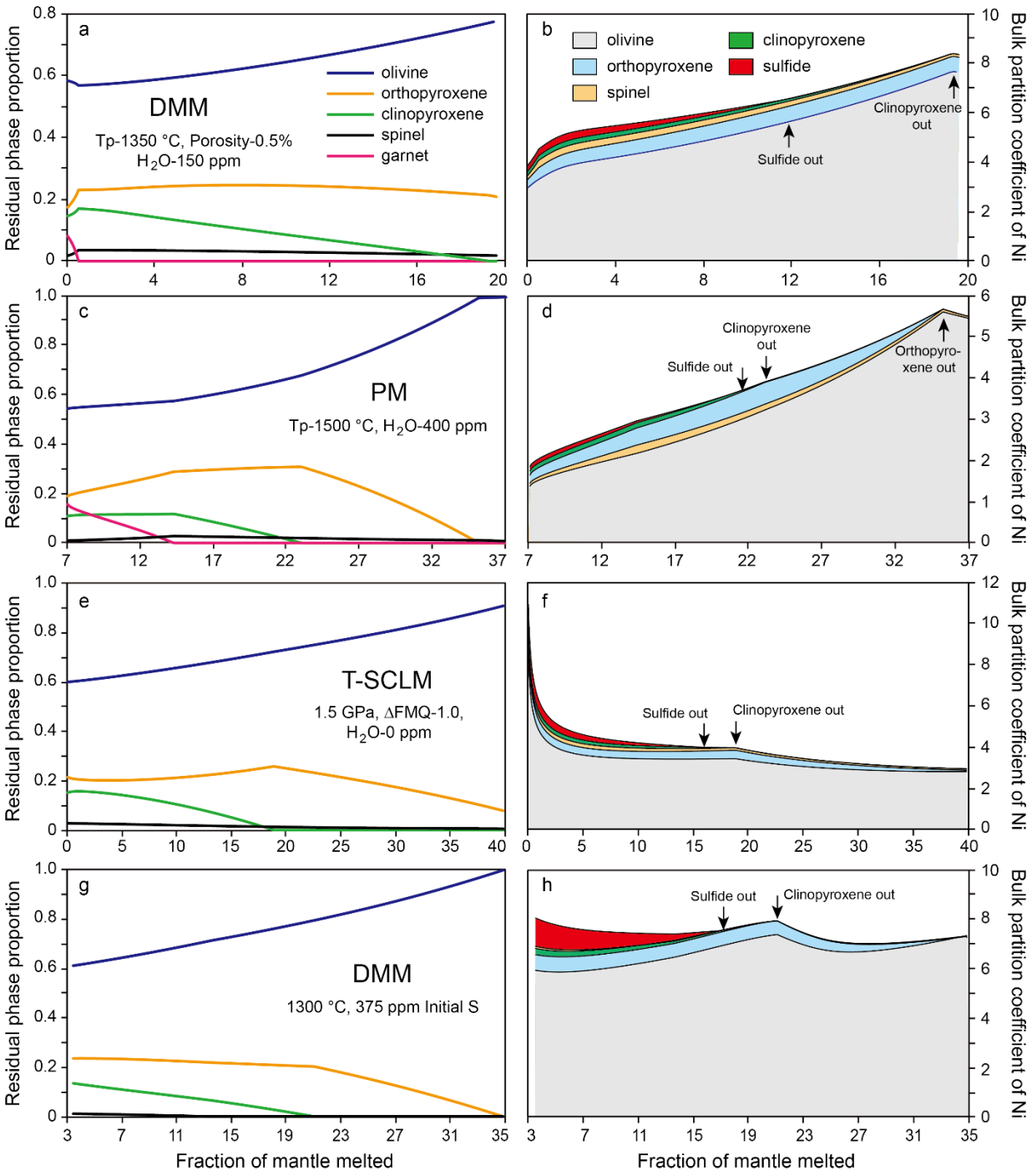


**Figure S6.** Weight fractions of residual crystalline phases in restite vs. weight fractions of mantle melted in alphaMELTS modeling for (**a**) polybaric continuous melting of DMM, (**c**) adiabatic decompression melting of PM, (**e**) isobaric melting of T-SCLM at 1.5 GPa and (**g**) flux-melting of mantle wedge at 1.0 GPa and 1300ºC. In addition, the variations and constitutions of the bulk partition coefficients of Ni between restite and silicate melt in each melting scenario were shown in (**b**) DMM, (**d**) PM, (**f**) T-SCLM and (**h**) mantle wedge.

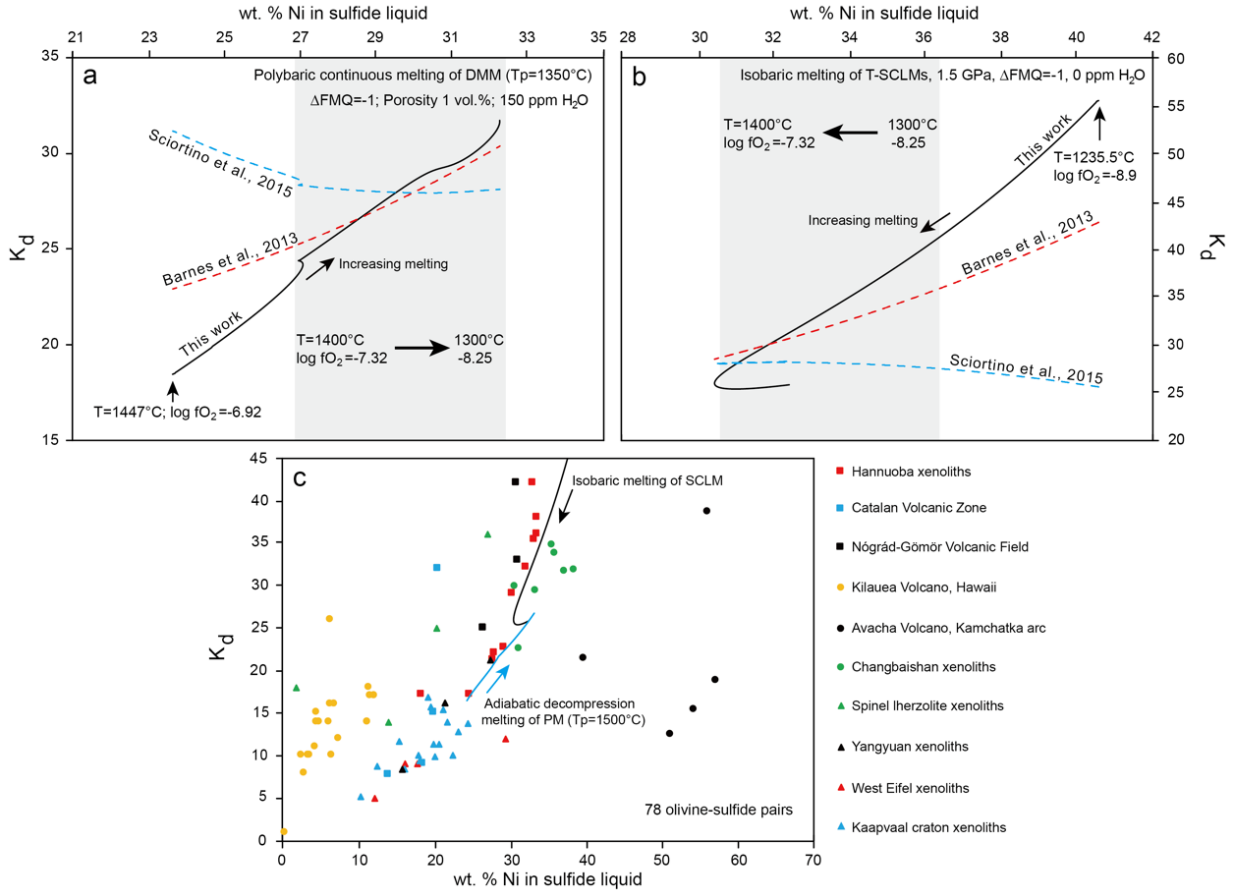


**Figure S7**. Evolutions of $K_d$ along with increasing melting for (**a**) polybaric continuous melting of DMM at 1350℃ $T_p$, (**b**) isobaric melting of T-SCLMs at 1.5 GPa. The blue and red dashed lines in (**a**) and (**b**) represent the results obtained from the $K_d$parameterizations of Sciortino et al. (2015) and Barnes et al. (2013), respectively. The gray vertical bands in (**a**) and (**b**) indicate the reference range where there are sufficient experimental data for $K_d$. (**c**). Values of $K_d$ and Ni wt. % from olivine-hosted sulfide inclusions in mantle peridotites. The blue and black lines exhibit the modeled evolution of $K_d$ during adiabatic decompression melting of PM ($T_p$=1500℃) and isobaric melting of SCLM, respectively. Data sources: Hannuoba and Yangyuan xenoliths, Liu et al. (2010); Catalan Volcanic Zone, Galán et al. (2016); Nógrád-Gömör Volcanic Field, Szabó and Bodnar (1995); Kilauea Volcano and spinel lherzolite xenoliths, Fleet and Stone (1990); Avacha Volcano, Kamchatka arc, Ishimaru and Arai (2008); Changbaishan xenoliths, Xu and Xie (2007); West Eifel xenoliths, Shaw (1997); Kaapvaal craton xenoliths, Lorand and Grégoire (2006).